

See discussions, stats, and author profiles for this publication at: <https://www.researchgate.net/publication/270340246>

The February 2014 Cephalonia Earthquake (Greece): 3D Deformation Field and Source Modeling from Multiple SAR Techn....

Article in *Seismological Research Letters* · November 2014

DOI: 10.1785/0220140126

CITATIONS

27

READS

368

11 authors, including:



John Peter Merryman Boncori

Technical University of Denmark

32 PUBLICATIONS 236 CITATIONS

[SEE PROFILE](#)



Ioannis Papoutsis

National Observatory of Athens

53 PUBLICATIONS 389 CITATIONS

[SEE PROFILE](#)



Giuseppe Pezzo

National Institute of Geophysics and Volcanology

43 PUBLICATIONS 193 CITATIONS

[SEE PROFILE](#)



C. Tolomei

National Institute of Geophysics and Volcanology

76 PUBLICATIONS 760 CITATIONS

[SEE PROFILE](#)

Some of the authors of this publication are also working on these related projects:



MARINE_EO [View project](#)



H2020 - Ever-est (European Virtual Environment for Research-Earth Science Themes) [View project](#)

The February 2014 Cephalonia Earthquake (Greece): 3D Deformation Field and Source Modeling from Multiple SAR Techniques

by John Peter Merryman Boncori, Ioannis Papoutsis, Giuseppe Pezzo, Cristiano Tolomei, Simone Atzori, Athanassios Ganas, Vassilios Karastathis, Stefano Salvi, Charalampos Kontoes, and A. Antonioli

Online Material: Tables of moment tensor elements; SAR image pairs and coseismic displacement gradients; figures of InSAR data, model parameter tradeoffs, and observed and modeled displacements.

INTRODUCTION

On 26 January 2014 at 13:55 UTC, an M_w 6.0 earthquake struck the island of Cephalonia, Greece, followed five hours later by an M_w 5.3 aftershock and by an M_w 5.9 event on 3 February 2014 at 03:08 UTC (National Observatory of Athens, Institute of Geodynamics [NOA-GI]). The epicenter of the M_w 6.0 event was relocated 2 km east of the town of Lixouri, and that of the M_w 5.9 event at the tip of the Gulf of Argostoli, in the northern part of the Paliki peninsula (Fig. 1; Karastathis *et al.*, 2014; Papadopoulos *et al.*, 2014). Extensive structural damage and widespread environmental effects were induced throughout the Paliki peninsula and along the eastern coast of the Gulf of Argostoli (Valkaniotis *et al.*, 2014). Quays, sidewalks, and piers were damaged in the waterfront areas of the towns of Lixouri and Argostoli, the island capital, and liquefactions, road failures, rock falls, and small landslides were observed. Most of the latter effects took place in the aftermath of the 26 January 2014 event and were reactivated one week later by the 3 February earthquake.

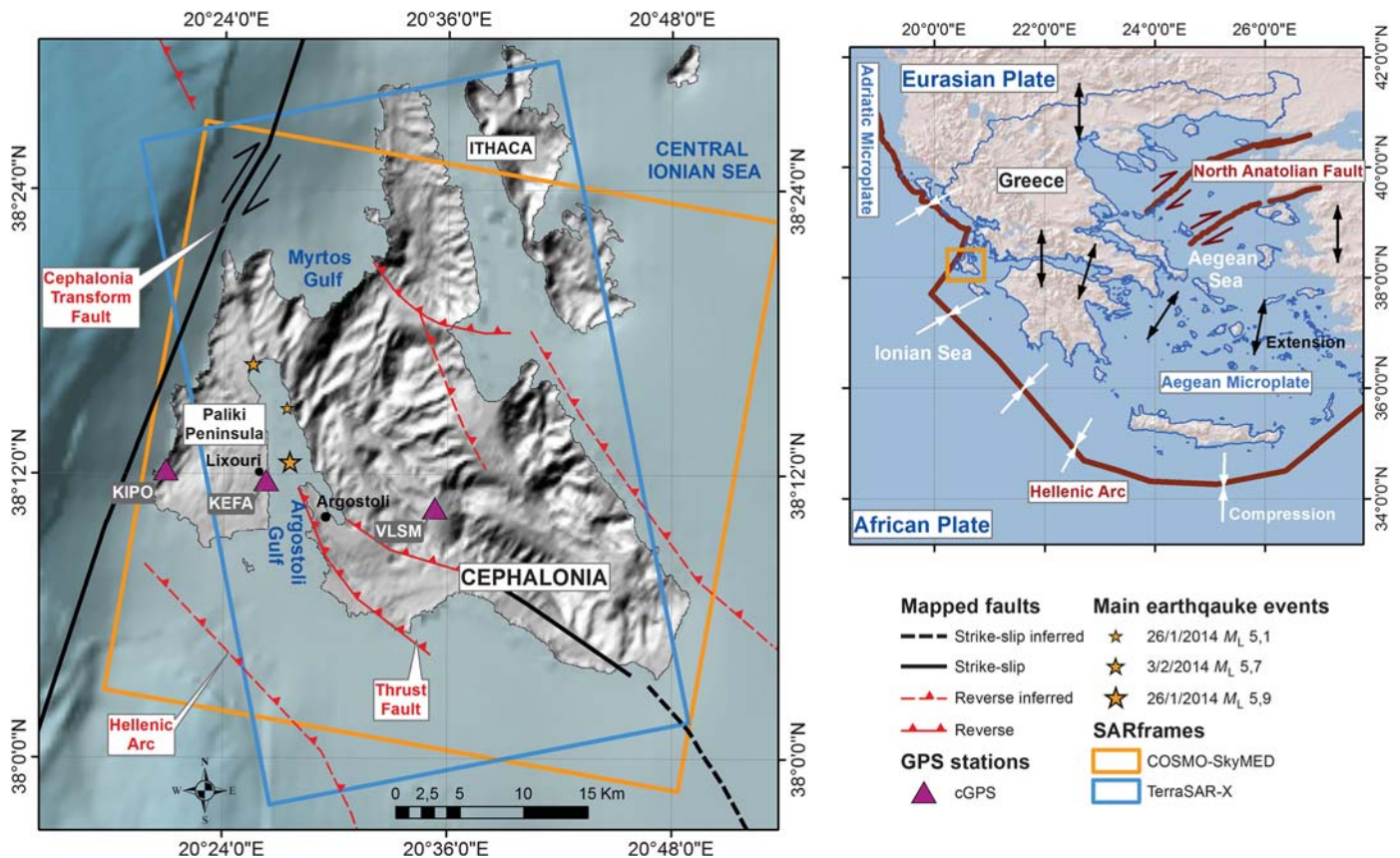
In this paper, we derive the 3D surface deformation field associated with the 3 February 2014 M_w 5.9 event based on the application of three different measurement techniques to Synthetic Aperture Radar (SAR) acquisitions from the Italian Space Agency (Agenzia Spaziale Italiana [ASI]) COSMO-SkyMed satellites and the German Aerospace Center (Deutsches Zentrum für Luft- und Raumfahrt, DLR) TANDem-X satellite. We then model the main seismic sources and their associated slip distributions, comparing the latter with improved hypocenter relocations, which allows us to speculate on the possible rupture mechanism. Finally, we discuss the contribution of our findings to the characterization of the seismogenic sources of this region.

TECTONIC FRAMEWORK

The island of Cephalonia is located in the central Ionian Sea (western Greece), which is a plate-boundary region dominated by the subduction of the Apulian (African) lithospheric plate with respect to the Aegean (Eurasian) one (Fig. 1). This takes place along the Hellenic arc, with current deformation rates varying between 25 mm/yr along its southern and central portions and 3–10 mm/yr along its northwestern margin (Hollenstein *et al.*, 2008; Pérouse *et al.*, 2012; Ganas *et al.*, 2013).

Seismically this region is characterized by continuous activity (<http://www.gein.noa.gr>; last accessed October 2014) and frequent occurrence of large earthquakes. In the last 500 years, events with an $M_s > 7.0$ have been recorded in 1469, 1636, 1743, 1767, 1867, 1953, and 1983 (Stiros *et al.*, 1994). In particular, the devastating M_w 7.0 event on 12 August 1953 and the preceding M_w 5.9 and M_w 6.6 events on 9 and 11 August 1953, respectively (Makropoulos *et al.*, 2012), destroyed more than 85% of the buildings in Cephalonia and all the buildings on the nearby islands of Ithaki and Zakynthos (Stiros *et al.*, 1994). Currently this region is assigned to the highest risk zone of the Greek seismic building code (Papagiannopoulos *et al.*, 2011).

Off the western coast of Cephalonia, right-lateral strike-slip faulting is the dominant mechanism, accommodating the transition between plate subduction and collision mechanisms at an oblique plate boundary (Fig. 1). A right-lateral fault system, known as the Cephalonia transform fault (CTF), has been suggested by several authors based on the analysis of seismological data (Scordilis *et al.*, 1985; Louvari *et al.*, 1999; Sachpazi *et al.*, 2000) and on deep seismic profiling surveys (Kokinou *et al.*, 2005, 2006). One of the segments of this fault is thought to be located about 10 km off the western coast of the island (Fig. 1). The CTF has been associated with some of the largest earthquakes of the past century in this area (Makropoulos *et al.*, 2012), including the M_w 6.7 and M_w 6.0 events on 17 January and 23 March 1983 southwest of Cephalonia (Scordilis *et al.*,



▲ **Figure 1.** Location map showing the tectonic context of the Aegean Sea and the main faults on the island of Cephalonia. Colored rectangles and magenta triangles indicate the Synthetic Aperture Radar (SAR) frame coverage and the continuous Global Positioning System (cGPS) stations, respectively. Yellow stars indicate the relocated epicenters of the three largest events of the 2014 sequence (Karastathis *et al.*, 2014). Diverging and converging arrows in the top-right map indicate approximate horizontal projections of the P axis (compression) and T axis (extension), respectively, based on figure 5b in Benetatos *et al.* (2004) and figure 1 in Karymbalis *et al.* (2013).

1985) and the 14 August 2003 M_w 6.2 event, west of the island of Lefkada (Benetatos *et al.*, 2005; Papathanassiou *et al.*, 2005). It is still a matter of debate whether the previously mentioned 1953 events were associated with the CTF (Papazachos *et al.*, 1994; Stiros *et al.*, 1994; Louvari *et al.*, 1999).

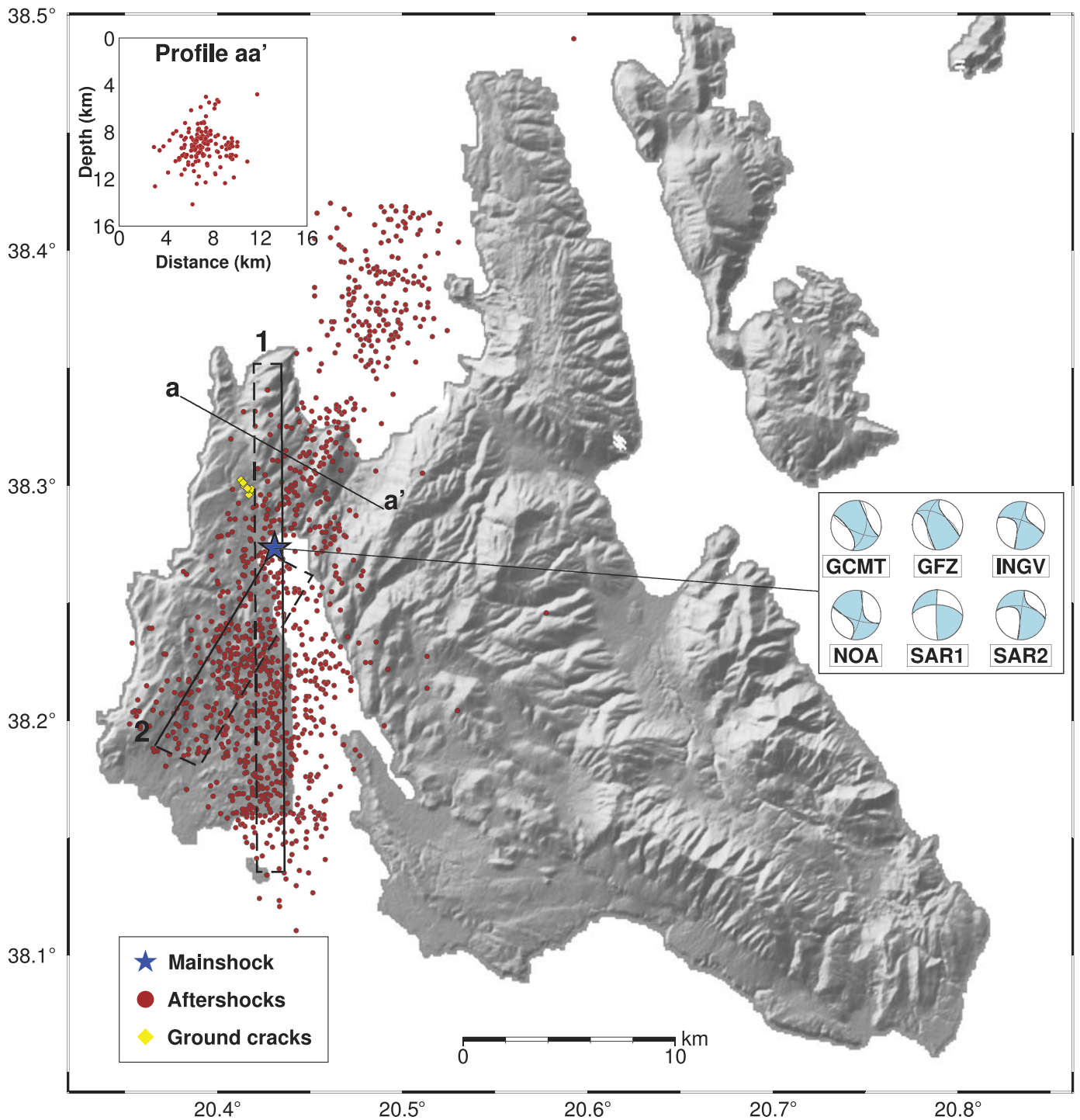
Onshore Cephalonia, thrust faulting is believed to be the predominant mechanism, along several faults of a thrust-and-fold belt dissecting the whole island (Fig. 1; Underhill, 1989). The activity of some of these faults is confirmed by seismological data (Tselentis *et al.*, 1997; Sachpazi *et al.*, 2000; Makropoulos *et al.*, 2012) and by Global Positioning System (GPS) measurements of internal deformations within the island (Lagios *et al.*, 2012).

THE 2014 SEISMIC SEQUENCE

The 26 January 2014 M_w 6.0 event was preceded by about a dozen small events ($M_L < 2.7$), mostly located north of the Paliki peninsula, and followed five hours later by an M_w 5.3 aftershock and by an M_w 5.9 event on 3 February 2014 (Karastathis *et al.*, 2014).

Hypocenters were initially determined by NOA-GI, using the Hellenic Unified Seismic Network (HUSN; <http://www.gein.noa.gr/en/networks/husn>; last accessed October 2014) and a 1D regional model of seismic wave velocities, used for daily seismicity analyses. Relocations were carried out with an improved velocity model based on Haslinger *et al.* (1999) and on information about the crustal structure of the wider area (Papazachos and Nolet, 1997), using the Nonlinloc software (Karastathis *et al.*, 2014). Figure 2 shows the relocated epicenters of 1130 events recorded between 3 February and 20 February 2014, which therefore include aftershocks from all three of the main events of the sequence.

The focal mechanisms provided by several geophysical institutes for the 3 February 2014 event are shown in Figure 2. The Global Centroid Moment Tensor (CMT) solution (<http://www.globalcmt.org/CMTsearch.html>; last accessed October 2014) was obtained by analyzing body, mantle, and surface waves from 147, 117, and 162 stations, respectively, with the method of Dziewonski *et al.* (1981) and Ekström *et al.* (2012). The GeoForschungsZentrum (GFZ) solution (<http://geofon.gfz-potsdam.de/eqinfo>; last accessed October 2014) is based on data from 247 GEOFON Extended Virtual Network



▲ **Figure 2.** Relocated epicenter of the 3 February 2014 event (blue star), earthquakes between 3 February and 20 February 2014 relocated by [Karastathis *et al.* \(2014\)](#) (red dots), ground cracks reported by [Valkaniotis *et al.* \(2014\)](#) following the 3 February 2014 event (yellow diamonds). Focal mechanisms for the 3 February 2014 event (Table 1) from seismological data (Global Centroid Moment Tensor [CMT], GeoForschungsZentrum [GFZ], Istituto Nazionale di Geofisica e Vulcanologia [INGV], National Observatory of Athens [NOA]) and from the synthetic moment tensors (© Table S3) calculated from the single-fault (SAR1) and two-fault inversions (SAR2) of SAR surface displacements discussed in the [Seismic Source Modeling](#) section. Black rectangles indicate the surface projection of the modeled fault planes discussed in [Seismic Source Modeling](#) section. Solid lines represent the intersection with topography (modeled fault traces). The top-left inset shows a vertical cross section along segment aa', computed with a 3 km wide buffer.

stations, analyzed with the approach of Saul *et al.* (2011). The Istituto Nazionale di Geofisica e Vulcanologia (INGV) solution (<http://cnt.rm.ingv.it/tdmt.html>; last accessed October 2014) was derived from the data of 15 stations (two located in southern Italy and the remaining ones in Greece), analyzed with the algorithm of Scognamiglio *et al.* (2009). Finally, the NOA solution was obtained from the data of nine Greek stations located to the north, east, and south of Cephalonia (<http://bbnet.gein.noa.gr>; last accessed October 2014) with the method of Sokos and Zahradnik (2008). Because of the location of Cephalonia at the eastern border of the Ionian sea (Fig. 1), the spatial distributions of the stations analyzed by INGV and NOA have large azimuthal gap angles of $\sim 180^\circ$.

In Table 1, we list the parameters of the best double-couple (DC) nodal planes more compatible with the regional tectonics. These consist of approximately north–south-striking planes with high dip angles, characterized by a main right-lateral mechanism and a smaller reverse component, with the exception of the GFZ solution, according to which these two mechanisms contribute almost equally. The plane is east dipping according to the Global CMT and NOA solutions and west dipping according to the GFZ and INGV ones. All mechanisms deviate from pure DC mechanisms (© Table S1, available in the electronic supplement to this article), with very low DC percentages for the solutions based on global networks (18% and 39% for the Global CMT and GFZ moment tensors, respectively) and

higher values for those based on regional networks (73% and 64% for the INGV and NOA solutions, respectively).

SURFACE DEFORMATION

SAR image pairs spanning the second mainshock of the sequence were acquired on descending and ascending passes, respectively, by the COSMO–SkyMed satellites on 2 February and 10 February 2014 and by the TanDEM-X satellite on 28 January and 8 February 2014. © Additional properties of these datasets are provided in Table S2. For each pass, coseismic surface displacements were measured along the radar line of sight (LoS; i.e., the direction of the shortest path between a point on ground and the SAR antenna phase center) and along the azimuth direction (i.e., the ground projection of the satellite flight path). LoS measurements were carried out with two different techniques: Differential SAR Interferometry (DInSAR; Massonnet and Feigl, 1995) and intensity tracking (ITR; Gray *et al.*, 1998). Azimuth measurements were carried out with ITR and with azimuth spectral diversity, also known as multi-aperture interferometry (MAI; Scheiber and Moreira, 2000; Behor and Zebker, 2006; Jung *et al.*, 2009). Processing was carried out with the GAMMA software package (Werner *et al.*, 2001).

The above-mentioned methods have several complementarities in terms of coverage, accuracy, and spatial resolution. For LoS measurements, although DInSAR is an order of mag-

Source	Latitude (°)	Longitude (°)	Length (km)	Width (km)	Top Depth (km)	Centroid Depth (km)	Strike (°)	Dip (°)	Rake (°)	Moment (10^{18} N·m)	M_w
Seismological Solutions											
Global CMT	38.07	20.37	—	—	—	12.0	12	57	157	1.33	6.0
GFZ	38.23	20.39	—	—	—	14.0	183	56	138	1.30	6.0
INGV	38.29	20.31	—	—	—	3.0	197	85	162	0.54	5.8
NOA	38.253	20.395	—	—	—	10.5	13	75	163	1.02	5.9
Inversion of SAR Measurements (This Study)											
<i>Single-Fault Model (SAR1)</i>											
Fault 1	$38.346 \pm 1.8 \times 10^{-03}$	$20.427 \pm 8.6 \times 10^{-04}$	24 ± 0.5	10 ± 1.1	0.5 ± 0.1	—	180 ± 1	86 ± 3	147 ± 3	1.41	6.0
<i>Two-Fault Model (SAR2)</i>											
Fault 1	38.346	20.427	24	10	0.5	—	180	86	147	0.95	5.9
	Fixed	Fixed	Fixed	Fixed	Fixed	—	Fixed	Fixed	Fixed	—	—
Fault 2	38.197	20.371	10	10	0.5	—	33	76	164	1.27	6.0
	Fixed	Fixed	Fixed	—	Fixed	—	Fixed	—	—	—	—
Total	—	—	—	—	—	—	—	—	—	2.22	6.2
The latitude and longitude columns represent the centroid coordinates for seismological sources and the top-left corners of the fault planes, respectively, for sources derived from the inversion of SAR measurements. For each source, only the nodal plane more compatible with the regional tectonics and the measured surface deformation is given. Errors stated for the SAR inversion parameters refer to the uniform slip model and represent error standard deviation values from a Monte Carlo error analysis (© Fig. S7).											

nitude more accurate than ITR, it requires the critical phase unwrapping step, which can potentially introduce large-scale errors up to tens of centimeters (Chen and Zebker, 2000). ITR does not require phase unwrapping and can be used to guide this step or cross validate its outcome (Joughin, 2002; Bamler and Eineder, 2005). It can also yield results in decorrelated areas, provided intensity features can be cross correlated (De Lange *et al.*, 2007). Concerning azimuth measurements, although MAI is more accurate than ITR for a given spatial resolution (Bamler and Eineder, 2005; Pezzo *et al.*, 2014) and does not typically require phase unwrapping, its applicability is restricted to areas with sufficient interferometric phase coherence.

DInSAR interferograms were generated on a 10 m posting for COSMO–SkyMed and on a 24 m posting for TanDEM-X, using a 5 m digital elevation model (DEM) from aerial photogrammetry to remove the topographic phase contribution. DEM coregistration was refined through the cross correlation of a simulated intensity image based on the DEM (Eineder, 2003) and the true radar intensity. Finally the filtering approach of Goldstein and Werner (1998) was applied with a $1 \text{ km} \times 1 \text{ km}$ spectral density estimation window and a constant α parameter of 0.8. To avoid large-scale phase unwrapping errors in both datasets, the Paliki peninsula had to be unwrapped separately from the rest of the island, due to an approximately north–south phase discontinuity associated with the coseismic deformation and stretching between the gulfs of Argostoli and Myrtos (Fig. 1). The two segments were bridged at a later stage, based on the unambiguous LoS measurements derived with ITR. MAI interferograms were generated on a 60 m posting and filtered using the approach of Goldstein and Werner (1998), which was applied with a 2 km spectral density estimation window and a constant α parameter of 0.8. ITR was carried out using cross-correlation window sizes of $400 \text{ m} \times 400 \text{ m}$ on ground. Because of the high resolution of the satellite imagery, it was essential to use the available DEM in the image coregistration step to avoid topography-correlated artifacts in the MAI and ITR results.

Application of the above-mentioned techniques to the COSMO–SkyMed and TanDEM-X datasets provided eight measurements of four independent displacement components, namely along the descending and ascending LoS and azimuth directions. Predicted error variances were generated with the method of Mohr and Merryman Boncori (2008), which provides a framework to exploit available models for the second-order statistics of error sources. We generalized the original method, which was proposed for DInSAR, extending it also to offset tracking and MAI. For DInSAR, the modeled error sources included decorrelation, DEM uncertainties, and tropospheric propagation, described by the midlatitude model of Merryman Boncori and Mohr (2008). For offset tracking, the variance of the offset estimates was modeled based on Joughin (2002), whereas MAI uncertainties due to decorrelation were modeled according to Bamler and Eineder (2005). Subsequently, a weighted least-squares inversion, with weights chosen as the inverse of the predicted error variances, was carried out to retrieve the Cartesian displacement components (east, north, and

up) for points for which at least one descending LoS, one ascending LoS, and one azimuth measurement (descending or ascending) was available. The Cartesian components, calculated on a $400 \text{ m} \times 400 \text{ m}$ posting, and the associated error standard deviations are shown in Figure 3, whereas the LoS and azimuth measurements, as well as the wrapped interferometric phase and coherence, are shown in ⊕ Figures S1–S6. The largest displacement gradients (up to 35 cm) are found in the north–south map (Fig. 3b) and indicate a right-lateral strike-slip component, in agreement with the focal mechanisms (Fig. 2; Table 1). Evidence for a reverse component is also found in the relative westward motion of the eastern part of the island toward the Paliki peninsula, as seen from the horizontal arrow field in Figure 3a–c, and in the relative upward motion (up to 20 cm) of Figure 3c.

The SAR-based deformations were validated against available continuous GPS (cGPS) stations (Fig. 1) within the coverage of at least one SAR data frame. These include VLSM and KIPO, which are part of NOANET (<http://www.gein.noa.gr/en/services/GPS>; last accessed October 2014), and the KEFA station, owned by the private Tree Company S.A., and for which data were provided by the National Technical University of Athens (NTUA) (<http://dionysos.survey.ntua.gr/src/kefallonia.htm>; last accessed October 2014). Coseismic measurements for the 3 February 2014 event were not available for the KIPO station due to a power outage. The data from VLSM and KEFA comprise daily 30 s observations and were analyzed using GAMIT/GLOBK 10.40 (Herring *et al.*, 2010). The recorded east and north coseismic displacements were 3.1 and -9.1 cm , respectively, for the KEFA station, and -1.6 and -0.9 cm , respectively, for the VLSM station.

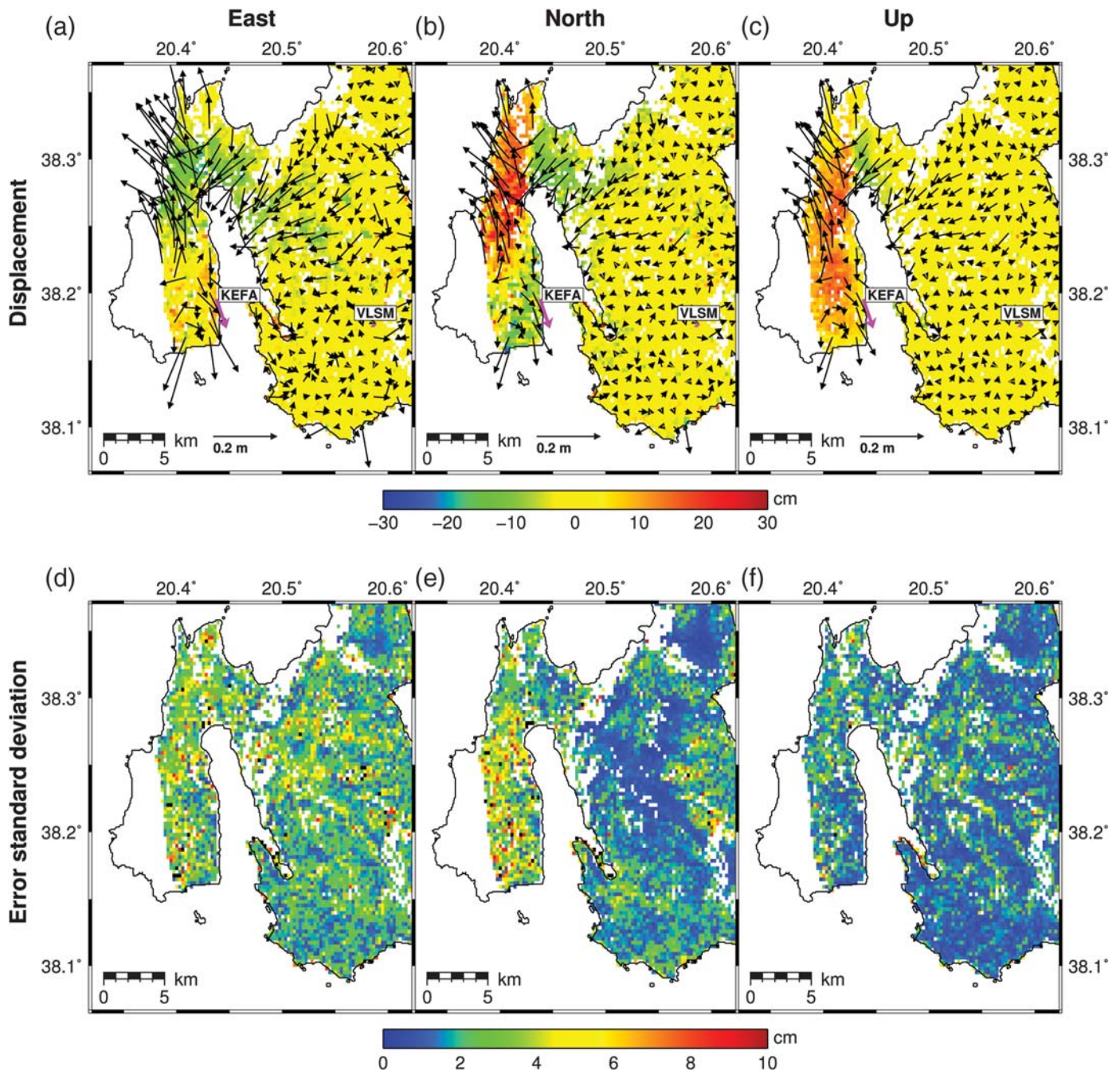
These values are in good agreement with those derived from SAR, as can be seen from Figure 3. For a quantitative comparison, because SAR measurements are relative in space, only the displacement gradient at the location of the two cGPS stations can be considered. The east and up components agree to within 1.5 cm, whereas the north components differ by less than 3 cm. These disagreements are explained by the predicted error standard deviation of the SAR and GPS measurements, which yield uncertainties for the differential measurements of about 3 cm for the east and north components and 4 cm for the up component (⊕ Table S3).

SEISMIC SOURCE MODELING

Single-Fault Model

We modeled the seismic source of the 3 February 2014 earthquake with a joint inversion of DInSAR, MAI, and ITR data, using the analytical solutions for dislocation in an elastic half-space (Okada, 1985). The eight input datasets were first subsampled to an irregularly spaced grid, with a posting varying between 200 and 500 m, respectively, in the nearfield and in the farfield. We then applied the approach of Atzori and Antonioli (2011).

First, a nonlinear inversion of the input datasets was carried out based on the Levenberg–Marquardt algorithm (Levenberg, 1944; Marquardt, 1963) to estimate the geometric and kinematic source parameters of a single-fault plane, assuming a



▲ **Figure 3.** (a) East, (b) north, and (c) up components of the coseismic displacement associated with the 3 February 2014 event. The arrow field represents the magnitude and direction of the horizontal displacement (east and north components) derived from the SAR measurements. The magenta arrows represent the horizontal displacements of the cGPS stations KEFA and VLSM. (d–f) East, north, and up displacement error standard deviations of the SAR measurements, respectively.

uniform slip. © The resulting parameter trade-offs and uncertainties are shown in Figure S7. Trade-offs occur between the top-depth, width, slip, strike, and rake parameters. The latter two are the most relevant, because the top-depth variations span a limited range (between 500 m and 1 km), and width and slip are refined in the subsequent linear inversion step. The strike and rake angles were optimized with a few iterations of the inversion procedure, in which only one of these parameters in turn was allowed to vary. The resulting source, hereafter re-

ferred to as fault 1, is a north–south-oriented near-vertical source characterized by transpressive kinematics, running parallel to the eastern coast of the Paliki peninsula and across the northern tip of the Argostoli Gulf (rectangle 1 in Fig. 2). Its parameters are given in Table 1, together with the uncertainties resulting from the nonlinear inversion.

Subsequently, we performed a linear inversion to retrieve the slip distribution (Atzori *et al.*, 2009), adopting a damped and non-negative least-squares approach (Menke, 1989). Slip

values were computed on a variable-size mesh, obtained with the approach of [Atzori and Antonioli \(2011\)](#), which maximizes the model resolution matrix ([Menke, 1989](#)). The width and length of the fault were adjusted at this stage to contain all patches with significant slip. For the study case, the patch sizes, which are automatically determined by the inversion algorithm, vary from 500 m at depths < 1 km to 5 km at depths > 5 km. Uncertainties (1σ predicted slip error standard deviation) were estimated with the approach described in appendix B of [Atzori et al. \(2008\)](#).

The slip distribution and uncertainties are shown in Figure 4. The north–south-oriented fault 1 shows an elongated pattern with significant slip in the upper 5 km, reaching the surface in its northernmost portion, corresponding to the northern tip of the Gulf of Argostoli. A maximum value of 1.76 m is found at a 4 km depth, 17 km along strike (Fig. 4b).

Figure 5 shows how the model reproduces the observed DInSAR LoS and MAI azimuth surface displacements. A similar plot is shown in [Figure S8](#) for the LoS and azimuth measurements, carried out with ITR at a lower spatial resolution. The overall median absolute deviations (MADs) of the residuals (observed minus modeled displacements) range from 1.5 cm for the more accurate DInSAR techniques to about 6 cm for the MAI and ITR azimuth measurements, with an average of 3.76 cm, taken over all eight measurements.

The model correctly reproduces the main LoS and azimuth displacement patterns in the north of the Paliki peninsula and in the area to the east of the modeled fault plane.

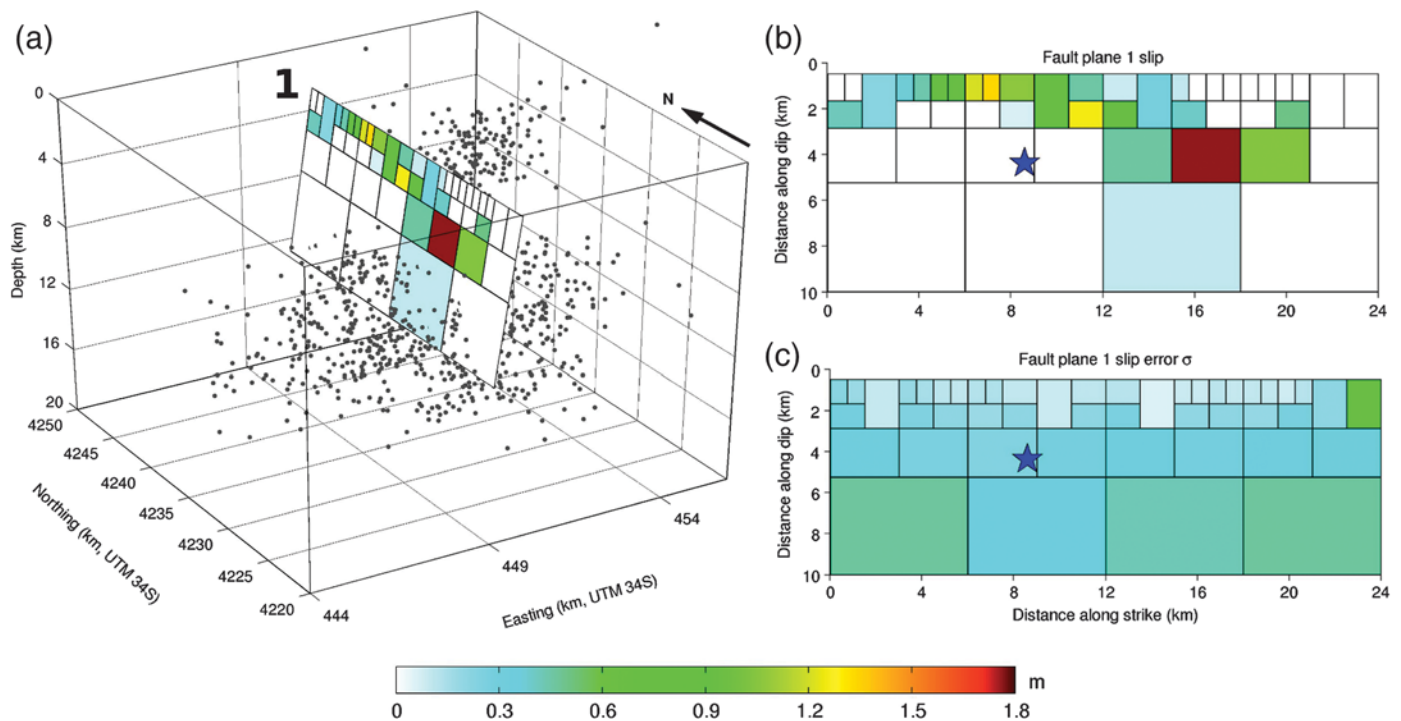
However, high residuals are found for all datasets in an area of about 50 km² in the south of the Paliki peninsula (gray rectangle in the third column of Figs. 5 and [Figure S8](#)). In particular, the model fails to explain a significant (~ 10 cm) southern motion component observed in both the descending (Figs. 5i and [Figure S8i](#)) and the ascending azimuth displacement maps (Figs. 5l and [Figure S8l](#)). Furthermore, it underestimates the descending LoS component by 5–10 cm (Figs. 5c and [Figure S8c](#)) and the ascending LoS component by ~ 6 cm (Figs. 5f and [Figure S8f](#)).

We find the model misfit cannot be significantly improved by fault parameter adjustments or variations in the slip distribution. Indeed a closer inspection of the north–south displacement map (Fig. 3b) points out an insurmountable limitation of the model, which is essentially that right-lateral rupture along a single-fault plane cannot simultaneously explain the southward displacement component of southeastern Paliki with respect to the eastern coast of the Gulf of Argostoli and its southward displacement with respect to the north of Paliki.

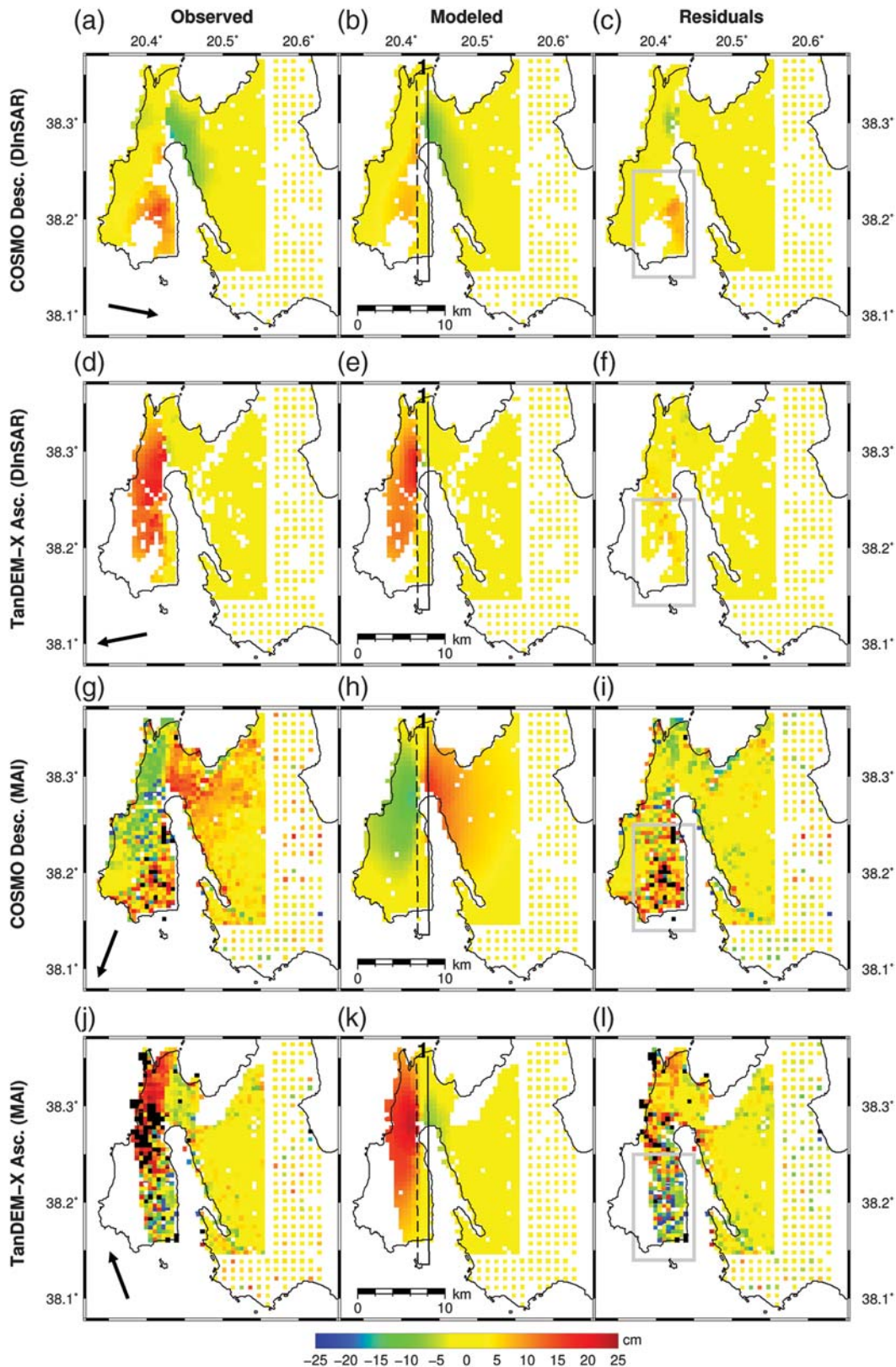
A solution to overcome the limitations of the single-fault model is to assume a second southwest-striking fault in southeastern Paliki (rectangle 2 in Fig. 2), as suggested by the location and orientation of the north–south displacement gradient in this area (Fig. 3b). We hereafter refer to this source as fault 2 and discuss the derivation of its parameters in the next section.

Two-Fault Model

The proximity of fault 1 to fault 2 implies that a nonlinear inversion to determine the parameters of both faults simulta-



▲ **Figure 4.** Slip distribution on the variable-size inversion mesh for the single-fault model of the seismic source of the 3 February 2014 event. (a) 3D view from southwest, (b) view perpendicular to the fault, (c) slip uncertainty (1σ) associated with fault 1. The blue star and the gray dots represent, respectively, the relocated hypocenter of the 3 February 2014 event and the aftershocks recorded between 3 February and 20 February 2014, after [Karastathis et al. \(2014\)](#).



▲ **Figure 5.** (Left) Observed, (middle) modeled, and (right) residual (observed minus modeled) displacements for the model discussed in the [Single-Fault Model](#) section. Sensor and measurement techniques (Differential SAR Interferometry [DInSAR] and multi aperture interferometry [MAI]) are reported to the left. The arrows in the first column indicate the direction of positive displacement and represent the ground projection of the line-of-sight vector and of the satellite flight path for DInSAR and MAI, respectively. The numbered black rectangle in the central column represents the modeled fault plane (fault 1).

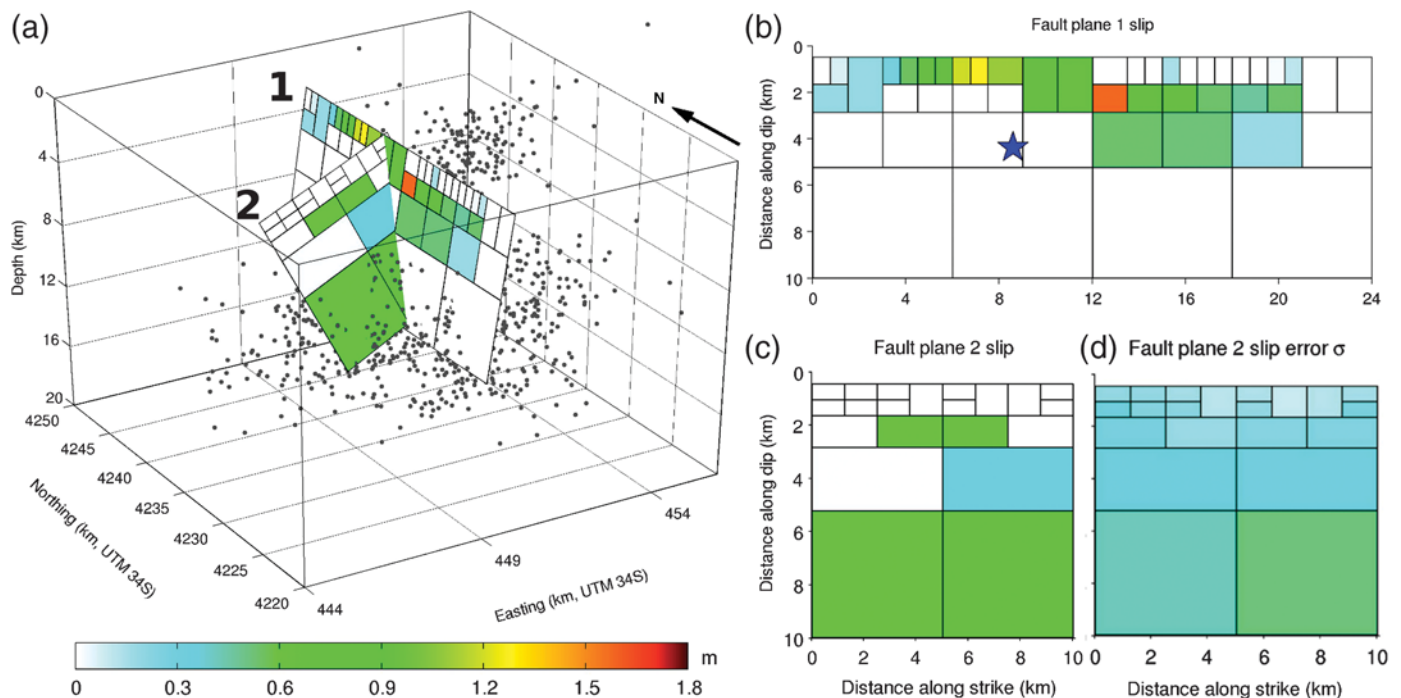
neously would lead to several trade-offs. We therefore solve only for uniform slip on both faults, and for the width, dip and rake of the second fault, using the same method described in the [Single-Fault Model](#) section. We hold the remaining faults 1 and 2 parameters fixed, as listed in Table 1, assigning the strike, location (latitude and longitude columns), and length of fault 2 based on the north–south displacements (Fig. 3b). We then iteratively refine the dip and rake angles of fault 2, by repeating the inversion, holding each parameter fixed in turn. The procedure converges on a solution with a high angle (dip = 76°) and dominant right-lateral strike-slip mechanism (rake = 164°). Finally, we carry out a linear inversion for the slip on both faults, computed on a variable-size mesh, following the same approach as in the [Single-Fault Model](#) section.

The resulting slip distributions are shown in Figure 6. For fault 1, a similar pattern to the single-fault case is found (Fig. 4b), although the maximum value of 1.6 m is slightly lower than in the single-fault case and is located at a shallower 3 km depth, 4 km more to the north (Fig. 6b). The northeast–southwest-oriented fault 2 has two relatively high slip patches (95 and 63 cm) at a 3 km depth. The slip distribution, however, is poorly resolved further at depth, and the modeling approach yields two large patches (5 km × 5 km) with an approximately 60 cm slip. We believe such poor resolution at depth to be due to the limited extent of the land surface above fault 2, which makes it impossible to constrain the farfield of the surface deformation. We therefore consider the slip distribution on fault 2 to be reliable only in the top 3 km, which is partly reflected by the increased slip uncertainties at depth in Figure 6d. The

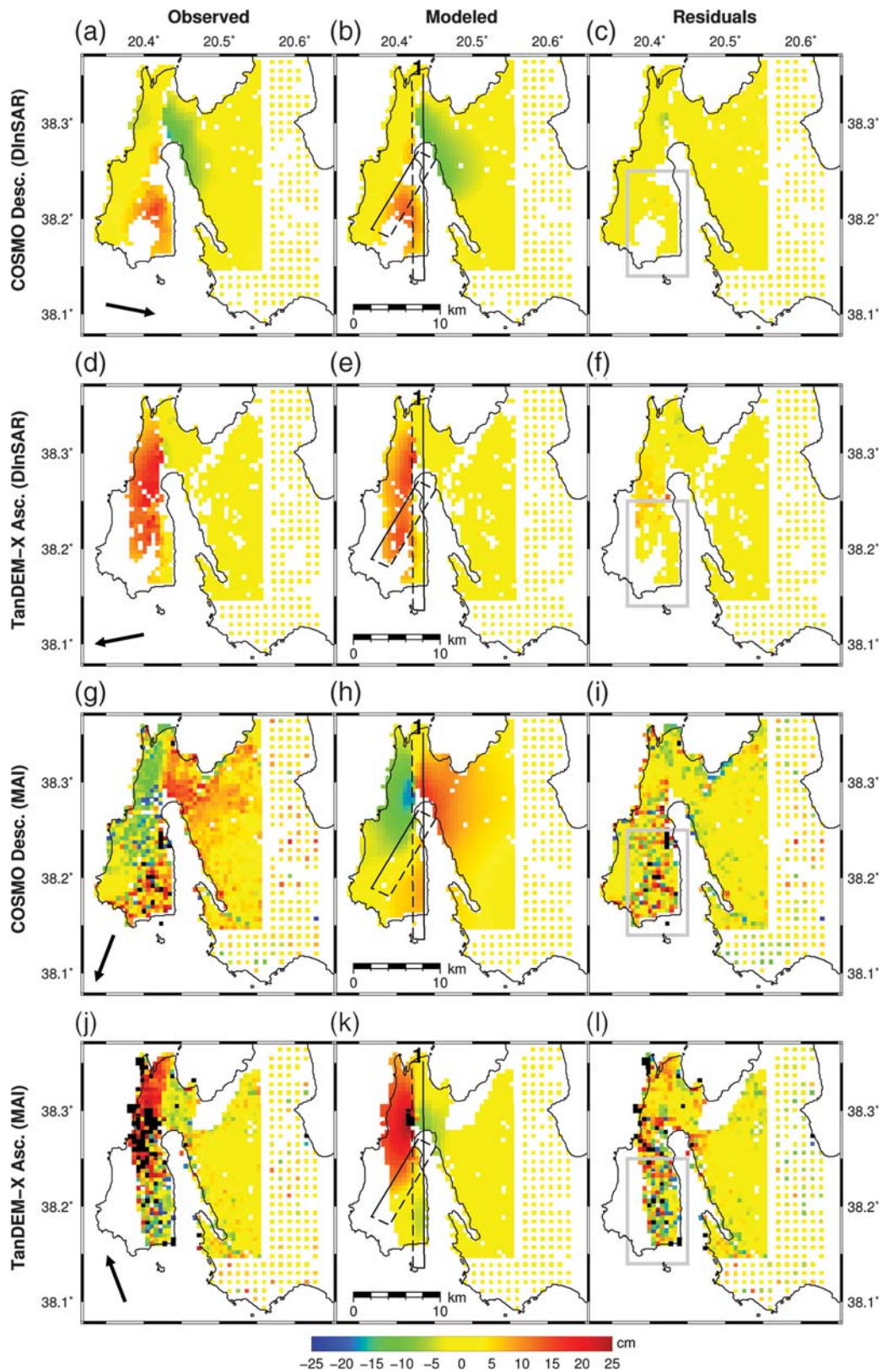
uncertainties of the fault 1 slip distribution are virtually identical to those of the single-fault model (Fig. 4c) and are not reported.

Figure 7 shows how the two-fault model reproduces the observed DInSAR LoS and MAI azimuth surface displacements. [Ⓔ](#) The same information is shown in Figure S9 for the lower-resolution ITR measurements. Comparing the DInSAR LoS displacement residual columns (Figs. 5c,f and 7c,f), the misfit of the descending and ascending LoS components has virtually disappeared, albeit for some local deviations; however, these are most likely due to phase unwrapping errors, particularly in the ascending pass interferogram. These local deviations are in fact not visible in the corresponding ITR LoS displacement residuals ([Ⓔ](#) Fig. S9c,f). However, these errors are limited in extent and magnitude (<6 cm) and do not have any significant impact on the modeled slip values. Also the azimuth displacements are better reproduced by the two-fault model (e.g., Figs. 5i,l and 7i,l, and in [Ⓔ](#) Figs. S8 and S9), although the right-lateral component in southern Paliki associated with fault 2 is still underestimated. Based on the synthetic azimuth displacements (Fig. 7h,k), it would seem that the fit could be improved by increasing the length of fault 2. However, due to the small extent of the surface displacement observations in this area, the constraints on the associated slip values would be poor.

The average MAD of the residuals (observed minus modeled displacements) over all datasets is 3.55 cm for the two-fault model, compared with 3.76 cm for the single-fault model. As seen from the residual histograms in [Ⓔ](#) Figure S10, the MADs of the two-fault model are lower or equal to those



▲ **Figure 6.** Slip distributions on the variable-size inversion mesh for the two-fault model of the seismic source of the 3 February 2014 event. (a) 3D view from southwest, (b,c) views perpendicular to each fault, and (d) slip uncertainty (1σ) associated with fault 2. The blue star and the gray dots, respectively, represent the relocated hypocenter of the 3 February 2014 event and the aftershocks recorded between 3 February and 20 February 2014, after [Karastathis et al. \(2014\)](#).



▲ **Figure 7.** The same as for Figure 5, but for the model discussed in the [Two-Fault Model](#) section.

of the single-fault model for all datasets except the descending DInSAR LoS. Comparing Figures 5c and 7c, this is probably due to a slight negative bias in the farfield of the modeled descending LoS displacement field (east of longitude 20.5).

Comparison with Seismically Derived Source Parameters

For each of the models derived in the [Single-Fault Model](#) and [Two-Fault Model](#) sections, we calculate the seismic moment as

$$M_0 = \mu \sum_i S_i W_i L_i$$

in which the summation is over the patches of the variable-size mesh of each fault, μ is the rigidity modulus, for which we assume a value of 30 GPa, and S_i , W_i , and L_i represent the slip, width, and length of the i th patch, respectively. For the single-fault model, we obtain a seismic moment of 1.41×10^{18} N·m, corresponding to an M_w of 6.0. Compared with the Global CMT value for instance (Table 1), we find a 6% disagreement, which is well within the expected variability range of SAR-based models compared with this specific catalog (e.g., fig. 4a in [Weston et al., 2011](#)). For the two-fault model, we instead find a moment of 2.22×10^{18} N·m, corresponding to an M_w of 6.2, which represents a significant overestimate compared with any of the seismological solutions. As seen in Table 1, however, this is due to the very high contribution of fault 2, which alone has a moment of 1.27×10^{18} N·m. In turn this value is largely influenced by the two deepest slip patches in Figure 6c, each with ~ 60 cm slip, which, as previously discussed, result from the incapability of our model to resolve the slip distribution at depth for this fault. If we exclude these patches from the fault 2 moment calculation, this decreases to 0.28×10^{18} N·m, yielding an overall moment of 1.23×10^{18} N·m for the two-fault model; this would be in the expected range of agreement with the Global CMT solution. This suggests that if it were possible to improve the slip resolution at depth for fault 2, the two-fault model also could yield a scalar moment compatible with that of the seismological solutions.

The geometric and kinematic parameters of our models are compared graphically with the seismological solutions in Figure 2, in which the SAR1 and SAR2 mechanisms refer to the single- and two-fault models, respectively. For the latter, the focal mechanism is computed from the full moment tensor (Table S1), obtained by summing the moment tensors of each planar fault. These in turn are computed from the parameters listed in Table 1, using equation (5), p. 243, of [Stein and Wysession \(2003\)](#). Figure 2 and Table 1 indicate that both SAR-based models are in better agreement with the NOA and INGV solutions, compared with those derived from global networks. Furthermore, the two-fault model presents a DC% of 64%, which is almost identical to the NOA value and similar to the INGV one (Table S1).

DISCUSSION

Surface deformation measurements spanning the 3 February 2014 M_w 5.9 event were derived with three different SAR

processing techniques, which when combined provide a good sensitivity to all Cartesian deformation components. Furthermore, for each LoS and azimuth measurement, two different techniques were applied, increasing the spatial coverage of the measurements and their robustness, in particular with respect to the DInSAR phase unwrapping processing step, which is particularly challenging for this site.

Although our measurements are not strictly coseismic, because they represent the cumulative deformation over the 8- to 11-day timespans of our SAR acquisitions (Table S2), the good agreement with coseismic cGPS measurements (Table S3) suggests the postseismic deformation associated with the two main events is actually a small percentage of the measured displacement (Fig. 3a–c) and lies below the measurement noise floor in epicentral areas (Fig. 3d–f).

To characterize the source of the 3 February 2014 event, we investigated both a single-fault and a two-fault model (Table 1). The majority of the observed surface deformation pattern (Fig. 3) can be explained by fault 1, a 20 km long north–south oriented and west-dipping structure running parallel to the east coast of the Paliki peninsula (Fig. 2) with a main right-lateral strike-slip mechanism and a lesser reverse component (rake = 147°). A second northeast–southwest fault (fault 2 in Table 1 and Fig. 2) has an even larger right-lateral strike-slip component (rake = 164°) and was found to significantly improve the fit to all observed displacements in the southeast of the Paliki peninsula (gray rectangles in the third column of Figs. 5 and 7 and of Figs. S8 and S9).

Both SAR-based models are consistent with the tectonic context of the western portion of the Hellenic arc subduction zone (Fig. 1). Their mechanisms show a greater agreement with those derived from regional seismic networks (NOA and INGV), as compared to those derived from global networks (Global CMT and GFZ) (Fig. 2; Table 1). The reasons for this, as well as for the differences between the seismically derived mechanisms themselves, are unknown and would be worth investigating further, because they could potentially contain information on the seismic source and/or on the rupture process. Inclusion of fault 2 in the model generates a moment tensor with a non-DC component of a comparable amount to that of the NOA and INGV solutions (Fig. 2; Table S1) and is consistent with the temporal evolution of the seismic sequence, which shows an increase in the seismicity of southeastern Paliki in the two weeks following the 3 February 2014 event (Fig. 2; [Karastathis et al., 2014](#)).

For both of the models derived in the [Single-Fault Model](#) and [Two-Fault Model](#) sections, the slip distribution on fault 1 is elongated and mostly contained within a depth of 5 km (Figs. 4b and 6b). Slip values become more superficial in the fault's northern portion, just above the tip of the Gulf of Argostoli, which is consistent with the field observations of [Valkaniotis et al. \(2014\)](#), who report an abundance of surface cracks in the north of Paliki (Fig. 2).

For the two-fault model, the slip distribution of fault 2 shows non-negligible values at a depth of about 2–3 km but is poorly resolved at greater depths, because most of the farfield

of the associated surface deformation is offshore. A consequence of this is that the two-fault model overestimates the total seismic moment (Table 1).

For both the single-fault and the two-fault models, the modeled slip distribution on fault 1 is in good agreement with the mainshock and aftershock relocations of Karastathis *et al.* (2014), both horizontally (Fig. 2) and at depth (Figs. 4 and 6). Based on Mai *et al.* (2005), for an M_w 5.9 strike-slip event, the hypocenter is expected to be horizontally well centered with respect to the slip distribution. Furthermore, it is expected to lie beneath the peak slip location and to be within a $0.15 R_{\max}$ distance from large slip asperities ($0.33\text{--}0.66 D_{\max}$) and a $0.5 R_{\max}$ distance from very large slip asperities ($>0.66 D_{\max}$), in which R_{\max} is the largest distance from the hypocenter to any point on the rupture plane and D_{\max} is the peak slip value. In relation to fault 1, for which $R_{\max} = 10$ km, these expectations are well satisfied for the two-fault model (Fig. 6b), for which $D_{\max} = 1.6$ m, whereas for the single-fault model (Fig. 4b), for which $D_{\max} = 1.76$ m, a closer distance between the hypocenter and the maximum slip value would be expected. For both models, the location of the hypocenter in areas of nominally zero slip is not considered critical, given the modeled slip error variance (Fig. 4c) and an ~ 1 km vertical uncertainty in the hypocenter location (Karastathis *et al.*, 2014). Concerning the apparent vertical bias of the aftershock cloud with respect to the slip distributions, two considerations are in order: (1) the cloud also includes aftershocks of the deeper 26 January 2014 events, and (2) our modeling approach assumes a homogeneous elastic half-space approximation, which, for shallow earthquakes, can lead to underestimations of the actual slip depth on the order of 10%–30% (Weston *et al.*, 2011, 2012 and references therein).

The location of the 3 February 2014 hypocenter with respect to the modeled slip distributions also suggests that the rupture nucleated on fault 1. The two-fault model would then imply a branching of the rupture. Although this occurs more frequently for larger earthquakes, branching has also been observed for moderate-size events, such as the M_w 6.1, 1985 Kettleman Hills event (Ekström *et al.*, 1992). Based on Kame *et al.* (2003), on pre-existing strike-slip faults with branches, the rupture properties depend on the angle between the main fault strike and the direction of the maximum pre-event compressive stress (Ψ), the angle between the main fault and the branch (φ), and the rupture velocity. In the case at hand, $\varphi = -30^\circ$ (Fig. 2), whereas reported Ψ values for Cephalonia lie between 60° (Hatzfeld *et al.*, 1989) and 80° (Benetatos *et al.*, 2004; Ganas *et al.*, 2013). For the 3 February 2014 event, assuming a pre-existing fault branch, branching is expected to occur to the west of the main fault and the rupture is expected to propagate on the main and the secondary branches, regardless of rupture velocity (compare to fig. 10, bottom row, in Kame *et al.*, 2003). Both of these aspects are in agreement with the two-fault modeling results, suggesting that branching would indeed be plausible based on the tectonic context. It would be interesting to investigate whether any evidence of fault 2 can be found in teleseismic

waveform data, as discussed by Jackson *et al.* (2006) for a secondary source of the 2003 Bam (Iran) earthquake.

Our study indicates that sources with a main right-lateral mechanism and a reverse component are also located onshore Cephalonia, and not only off its western coast, although further studies are required to understand the connection at depth of these sources with the CTF and/or the east-dipping thrust faults of the thrust-and-fold belt dissecting the island.

Finally, we note the main deformation pattern observed for the 3 February 2014 event, namely the relative uplift and north-northeast motion of the Paliki peninsula with respect to the mainland (Fig. 3a–c), shows some interesting similarities with the GPS measurements carried out by Lagios *et al.* (2012) for the 2003–2010 time span. The latter reports relative north-northeast horizontal motion rates up to 8 mm/yr and relative uplift rates between 5 and 11 mm/yr of the Paliki peninsula, with respect to the central part of the island. To understand if there can be any connection between these measurements and the main ruptures of the Cephalonia 2014 seismic sequence, it would be of great interest to continue monitoring the internal deformation rates of the island in the following years and to model the source of the 26 January 2014 event. 

ACKNOWLEDGMENTS

COSMO–SkyMed products were provided under license by the Italian Space Agency (Agenzia Spaziale Italiana [ASI]), as a contribution to Objective C of the Committee on Earth Observation Satellites Disaster Risk Management (CEOS DRM) seismic pilot. TanDEM-X data were provided by the German Aerospace Center (Deutsches Zentrum für Luft- und Raumfahrt) in the framework of the GEO1986 project. Coseismic values for continuous Global Positioning System (cGPS) station VLSM were provided by Kostas Chousianitis (National Observatory of Athens). Data from cGPS station KEFA, owned by Tree Company S.A., were provided by the National Technical University of Athens (<http://dionysos.survey.ntua.gr/>; last accessed October 2014). Several figures were prepared using the public-domain Generic Mapping Tool software (Wessel and Smith, 1998). J. P. Merryman Boncori and G. Pezzo were funded by the ASI– Istituto Nazionale di Geofisica e Vulcanologia (INGV) MuSA project. I. Papoutsis was supported by the FP7 EU project BEYOND (GA 316210). We thank L. Scognamiglio and E. Tinti for the fruitful discussions and an anonymous reviewer whose constructive comments improved the quality of the manuscript.

REFERENCES

- Atzori, S., and A. Antonioli (2011). Optimal fault resolution in geodetic inversion of coseismic data, *Geophys. J. Int.* **185**, no. 1, 529–538, doi: [10.1111/j.1365-246X.2011.04955.x](https://doi.org/10.1111/j.1365-246X.2011.04955.x).
- Atzori, S., I. Hunstad, M. Chini, S. Salvi, C. Tolomei, C. Bignami, S. Stramondo, E. Trasatti, A. Antonioli, and E. Boschi (2009). Finite fault inversion of DInSAR coseismic displacement of the 2009 L'Aquila earthquake (central Italy), *Geophys. Res. Lett.* **36**, no. 15, L15305, doi: [10.1029/2009GL039293](https://doi.org/10.1029/2009GL039293).

- Atzori, S., M. Manunta, G. Fornaro, A. Ganas, and S. Salvi (2008). Post-seismic displacement of the 1999 Athens earthquake retrieved by the Differential Interferometry by Synthetic Aperture Radar time series, *J. Geoph. Res.* **113**, no. B9, doi: [10.1029/2007JB005504](https://doi.org/10.1029/2007JB005504).
- Bamler, R., and M. Eineder (2005). Accuracy of differential shift estimation by correlation and split-bandwidth interferometry for wide-band and delta-k SAR systems, *Geosci. Remote Sens. Lett.* **2**, no. 2, 151–155, doi: [10.1109/LGRS.2004.843203](https://doi.org/10.1109/LGRS.2004.843203).
- Bechor, N. B. D., and H. A. Zebker (2006). Measuring two-dimensional movements using a single InSAR pair, *Geophys. Res. Lett.* **33**, L16311, doi: [10.1029/2006GL026883](https://doi.org/10.1029/2006GL026883).
- Benetatos, C., A. Kiratzi, C. Papazachos, and G. Karakaisis (2004). Focal mechanisms of shallow and intermediate depth earthquakes along the Hellenic arc, *J. Geodyn.* **37**, no. 2, 253–296, doi: [10.1016/j.jog.2004.02.002](https://doi.org/10.1016/j.jog.2004.02.002).
- Benetatos, C., A. Kiratzi, Z. Roumelioti, G. Stravarakakis, G. Drakatos, and I. Latoussakis (2005). The 14 August 2003 Lefkada island (Greece) earthquake: Focal mechanisms of the mainshock and of the aftershock sequence, *J. Seismol.* **9**, no. 2, 171–190, doi: [10.1007/s10950-005-7092-1](https://doi.org/10.1007/s10950-005-7092-1).
- Chen, C. W., and H. A. Zebker (2000). Network approaches to two-dimensional phase unwrapping: Intractability and two new algorithms, *J. Opt. Soc. Am. A* **17**, no. 3, 401–414, doi: [10.1364/JOSAA.17.000401](https://doi.org/10.1364/JOSAA.17.000401).
- De Lange, R., A. Luckman, and T. Murray (2007). Improvement of satellite radar feature tracking for ice velocity derivation by spatial frequency filtering, *IEEE Trans. Geosci. Remote Sens.* **45**, no. 7, 2309–2318, doi: [10.1109/TGRS.2007.896615](https://doi.org/10.1109/TGRS.2007.896615).
- Dziewonski, A. M., T.-A. Chou, and J. H. Woodhouse (1981). Determination of earthquake source parameters from waveform data for studies of global and regional seismicity, *J. Geophys. Res.* **86**, 2825–2852, doi: [10.1029/JB086iB04p02825](https://doi.org/10.1029/JB086iB04p02825).
- Eineder, M. (2003). Efficient simulation of SAR interferograms of large areas and of rugged terrain, *IEEE Trans. Geosci. Remote Sens.* **41**, no. 6, 1415–1427, doi: [10.1109/TGRS.2003.811692](https://doi.org/10.1109/TGRS.2003.811692).
- Ekström, G., M. Nettles, and A. M. Dziewonski (2012). The Global CMT project 2004–2010: Centroid-moment tensors for 13,017 earthquakes, *Phys. Earth Planet. In.* **200/201**, 1–9, doi: [10.1016/j.pepi.2012.04.002](https://doi.org/10.1016/j.pepi.2012.04.002).
- Ekström, G., R. S. Stein, J. P. Eaton, and D. Eberhart-Phillips (1992). Seismicity and geometry of a 110 km-long blind thrust fault. 1. The 1985 Kettleman Hills, California, earthquake, *J. Geophys. Res.* **97**, no. B4, 4843–4864, doi: [10.1029/91JB02925](https://doi.org/10.1029/91JB02925).
- Ganas, A., A. Marinou, D. Anastasiou, D. Paradissis, K. Papazissi, P. Tzavaras, and G. Drakatos (2013). GPS-derived estimates of crustal deformation in the central and north Ionian Sea, Greece: 3-yr results from NOANET continuous network data, *J. Geodyn.* **67**, 62–71, doi: [10.1016/j.jog.2012.05.010](https://doi.org/10.1016/j.jog.2012.05.010).
- Goldstein, R. M., and C. L. Werner (1998). Radar interferogram filtering for geophysical applications, *Geophys. Res. Lett.* **25**, no. 21, 4035–4038, doi: [10.1029/1998GL900033](https://doi.org/10.1029/1998GL900033).
- Gray, A. L., K. E. Mattar, and P. W. Vachon (1998). InSAR results from the RADARSAT Antarctic mapping mission data: Estimation of glacier motion using a simple registration procedure, in *Proc. Geosc. and Rem. Sens. Symposium (IGARSS'98)*, Seattle, Washington, 6–10 July 1998, 1638–1640, doi: [10.1109/IGARSS.1998.691662](https://doi.org/10.1109/IGARSS.1998.691662).
- Haslinger, F., E. Kissling, J. Ansoerge, D. Hatzfeld, E. Papadimitriou, V. Karakostas, K. Makropoulos, H. G. Kahle, and Y. Peter (1999). 3D crustal structure from local earthquake tomography around the Gulf of Arta (Ionian region, NW Greece), *Tectonophysics* **304**, 201–218, doi: [10.1016/S0040-1951\(98\)00298-4](https://doi.org/10.1016/S0040-1951(98)00298-4).
- Hatzfeld, D., G. Pedotti, P. Hatzidimitriou, and K. Makropoulos (1989). The strain pattern in the western Hellenic arc deduced from a microearthquake survey, *Geophys. J. Int.* **101**, no. 1, 181–202, doi: [10.1111/j.1365-246X.1990.tb00767.x](https://doi.org/10.1111/j.1365-246X.1990.tb00767.x).
- Herring, T. A., R. W. King, and S. McClusky (2010). *Documentation for the GAMIT/GLOBK GPS Processing Software Release 10.4*, Massachusetts Institute of Technology, Cambridge.
- Hollenstein, C., M. D. Müller, A. Geiger, and H. G. Kahle (2008). Crustal motion and deformation in Greece from a decade of GPS measurements, 1993–2003, *Tectonophysics* **449**, nos. 1/4, 17–40, doi: [10.1016/j.tecto.2007.12.006](https://doi.org/10.1016/j.tecto.2007.12.006).
- Jackson, J., M. Bouchon, E. Fielding, G. Funning, M. Ghorashi, D. Hatzfeld, H. Nazari, B. Parsons, K. Priestly, M. Talebian, M. Tatar, R. Walker, and T. Wright (2006). Seismotectonic, rupture process, and earthquake-hazard aspects of the 2003 December 26 Bam, Iran, earthquake, *Geophys. J. Int.* **166**, no. 3, doi: [10.1111/j.1365-246X.2006.03056.x](https://doi.org/10.1111/j.1365-246X.2006.03056.x).
- Joughin, I. (2002). Ice-sheet velocity mapping: A combined interferometric and speckle-tracking approach, *Ann. Glaciol.* **34**, no. 1, 195–201, doi: [10.3189/172756402781817978](https://doi.org/10.3189/172756402781817978).
- Jung, H. S., J. S. Won, and S. W. Kim (2009). An improvement of the performance of multiple-aperture SAR interferometry (MAI), *IEEE Trans. Geosci. Remote Sens.* **47**, no. 8, 2859–2869, doi: [10.1109/TGRS.2009.2016554](https://doi.org/10.1109/TGRS.2009.2016554).
- Kame, N., J. R. Rice, and R. Dmowska (2003). Effects of prestress state and rupture velocity on dynamic fault branching, *J. Geophys. Res.* **108**, no. B5, ESE 13-1–13-21, doi: [10.1029/2002JB002189](https://doi.org/10.1029/2002JB002189).
- Karastathis, V. K., E. Mouzakiotis, A. Ganas, and G. A. Papadopoulos (2014). High-precision relocation of seismic sequences above a dipping Moho: The case of the January-February 2014 seismic sequence in Cephalonia Isl. (Greece), *Solid Earth Discuss.* **6**, 2699–2733, doi: [10.5194/sed-6-2699-2014](https://doi.org/10.5194/sed-6-2699-2014).
- Karymbalis, E., D. Papanastassiou, K. Gaki-Papanastassiou, K. Tsanakas, and H. Maroukian (2013). Geomorphological study of Cephalonia Island, Ionian Sea, western Greece, *J. Maps* **9**, no. 1, 121–134, doi: [10.1080/17445647.2012.758423](https://doi.org/10.1080/17445647.2012.758423).
- Kokinou, E., E. Kamberis, A. Vafidis, D. Monopolis, G. Ananiadis, and A. Zelelidis (2005). Deep seismic reflection data from offshore western Greece: A new crustal model for the Ionian Sea, *J. Petrol. Geol.* **28**, no. 2, 185–202, doi: [10.1111/j.1747-5457.2005.tb00079.x](https://doi.org/10.1111/j.1747-5457.2005.tb00079.x).
- Kokinou, E., E. Papadimitriou, V. Karakostas, E. Kamberis, and F. Vallianatos (2006). The Kefalonia transform zone (offshore western Greece) with special emphasis to its prolongation towards the Ionian abyssal plain, *Mar. Geophys. Res.* **27**, no. 4, 241–252, doi: [10.1007/s11001-006-9005-2](https://doi.org/10.1007/s11001-006-9005-2).
- Lagjos, E., P. Papadimitriou, F. Novali, V. Sakkas, A. Fumagalli, K. Vlachou, and S. Del Conte (2012). Combined seismicity pattern analysis, DGPd and PSInSAR studies in the broader area of Cephalonia (Greece), *Tectonophysics* **524/525**, 43–58, doi: [10.1016/j.tecto.2011.12.015](https://doi.org/10.1016/j.tecto.2011.12.015).
- Levenberg, K. (1944). A method for the solution of certain non-linear problems in least squares, *Q. J. Appl. Math.* **2**, 164–168.
- Louvari, E., A. A. Kiratzi, and B. C. Papazachos (1999). The CTF and its extension to western Lefkada Island, *Tectonophysics* **308**, 223–236, doi: [10.1016/S0040-1951\(99\)00078-5](https://doi.org/10.1016/S0040-1951(99)00078-5).
- Mai, P. M., P. Spudich, and J. Boatwright (2005). Hypocenter locations in finite-source rupture models, *Bull. Seismol. Soc. Am.* **95**, no. 3, 965–980, doi: [10.1785/0120040111](https://doi.org/10.1785/0120040111).
- Makropoulos, K., G. Kaviris, and V. Kouskouna (2012). An updated and extended earthquake catalogue for Greece and adjacent areas since 1900, *Nat. Hazards Earth Syst. Sci.* **12**, 1425–1430, doi: [10.5194/nhess-12-1425-2012](https://doi.org/10.5194/nhess-12-1425-2012).
- Marquardt, D. (1963). An algorithm for least-squares estimation of non-linear parameters, *SIAM J. Appl. Math.* **11**, 431–441.
- Massonnet, D., and K. L. Feigl (1995). Discrimination of geophysical phenomena in satellite radar interferograms, *Geophys. Res. Lett.* **22**, no. 12, 1537–1540, doi: [10.1029/95GL00711](https://doi.org/10.1029/95GL00711).
- Menke, W. (1989). *Geophysical Data Analysis: Discrete Inverse Theory*, Academic Press, San Diego, California.
- Merryman Boncori, J. P., and J. J. Mohr (2008). A tunable closed-form model for the structure function of tropospheric delay, *Geosci. Remote Sens. Lett.* **5**, no. 2, 222–226, doi: [10.1109/LGRS.2008.915738](https://doi.org/10.1109/LGRS.2008.915738).
- Mohr, J. J., and J. P. Merryman Boncori (2008). An error prediction framework for interferometric SAR data, *IEEE Trans. Geosci. Remote Sens.* **46**, no. 6, 1600–1613, doi: [10.1109/TGRS.2008.916213](https://doi.org/10.1109/TGRS.2008.916213).

- Okada, Y. (1985). Surface deformation due to shear and tensile faults in a half-space, *Bull. Seismol. Soc. Am.* **75**, no. 4, 1135–1154.
- Papadopoulos, G. A., V. K. Karastathis, I. Koukouvelas, M. Sachpazi, I. Baskoutas, G. Chouliaras, A. Agalos, E. Daskalaki, G. Minidakis, A. Moshou, A. Mouzakiotis, K. Orfanogiannaki, A. Papageorgiou, D. Spanos, and I. Triatafyliou (2014). The Cephalonia, Ionian Sea (Greece), sequence of strong earthquakes of January–February 2014: A first report, *Res. Geophys.* **4**, no. 1, doi: [10.4081/rg.2014.5441](https://doi.org/10.4081/rg.2014.5441).
- Papagiannopoulos, G. A., G. D. Hatzigeorgiou, and D. E. Beskos (2011). An assessment of seismic hazard and risk in the islands of Cephalonia and Ithaca, Greece, *Soil Dynam. Earthq. Eng.* **32**, 15–25, doi: [10.1016/j.soildyn.2011.08.001](https://doi.org/10.1016/j.soildyn.2011.08.001).
- Papathanassiou, G., S. Pavlides, and A. Ganas (2005). The 2003 Lefkada earthquake: Field observations and preliminary microzonation map based on liquefaction potential index for the town of Lefkada, *Eng. Geol.* **82**, no. 1, 12–31, doi: [10.1016/j.enggeo.2005.08.006](https://doi.org/10.1016/j.enggeo.2005.08.006).
- Papazachos, B. C., G. F. Karakaisis, and P. P. Hatzidimitriou (1994). Further information on the transform fault of the Ionian sea, *XXIV General Assembly of the European Seismology Commission*, Athens, Greece, 19–24 September, 12 pp.
- Papazachos, C. B., and G. Nolet (1997). P and S deep velocity structure of the Hellenic area obtained by robust nonlinear inversion of travel times, *J. Geophys. Res.* **102**, no. B4, 8349–8367, doi: [10.1029/96JB03730](https://doi.org/10.1029/96JB03730).
- Pérouse, E., N. Chamot-Rooke, A. Rabaute, P. Briole, F. Jouanne, I. Georgiev, and D. Dimitrov (2012). Bridging onshore and offshore present-day kinematics of central and eastern Mediterranean: implications for crustal dynamics and mantle flow, *Geochem. Geophys. Geosyst.* **13**, Q09013, doi: [10.1029/2012GC004289](https://doi.org/10.1029/2012GC004289).
- Pezzo, G., J. P. Merryman Boncori, S. Atzori, A. Antonioli, and S. Salvi (2014). Deformation of the western Indian Plate boundary: Insights from differential and multi-aperture InSAR data inversion for the 2008 Baluchistan (western Pakistan) seismic sequence, *Geophys. J. Int.* **197**, no. 3, doi: [10.1093/gji/ggu106](https://doi.org/10.1093/gji/ggu106).
- Sachpazi, M., A. Hirn, C. Clement, F. Haslinger, M. Laigle, E. Kissling, P. Charvis, Y. Hello, J. C. Lepine, M. Sapin, and J. Ansorge (2000). Western Hellenic subduction and Cephalonia transform: Local earthquakes and plate transport and strain, *Tectonophysics* **319**, no. 4, 301–319, doi: [10.1016/S0040-1951\(99\)00300-5](https://doi.org/10.1016/S0040-1951(99)00300-5).
- Saul, J., J. Becjer, and W. Hanka (2011). Global moment tensor computation at GFZ Potsdam, paper presented at *AGU 2011 Fall Meeting*, San Francisco, California, 5–9 December 2011.
- Scheiber, R., and A. Moreira (2000). Coregistration of interferometric SAR images using spectral diversity, *IEEE Trans. Geosci. Remote Sens.* **38**, no. 5, 2179–2191, doi: [10.1109/36.868876](https://doi.org/10.1109/36.868876).
- Scognamiglio, L., E. Tinti, and A. Michelini (2009). Real-time determination of seismic moment tensor for the Italian region, *Bull. Seismol. Soc. Am.* **99**, 2223–2242, doi: [10.1785/0120080104](https://doi.org/10.1785/0120080104).
- Scordilis, E. M., G. F. Karakaisis, B. G. Karakostas, D. G. Panagiotopoulos, P. E. Comninakis, and B. C. Papazachos (1985). Evidence for transform faulting in the Ionian Sea: The Cephalonia Island earthquake sequence of 1983, *Pure Appl. Geophys.* **123**, no. 3, 388–397, doi: [10.1007/BF00880738](https://doi.org/10.1007/BF00880738).
- Sokos, E. N., and J. Zahradnik (2008). ISOLA a FORTRAN code and a MATLAB GUI to perform multiple-point source inversion of seismic data, *Comput. Geosci.* **24**, 967–977, doi: [10.1016/j.cageo.2007.07.005](https://doi.org/10.1016/j.cageo.2007.07.005).
- Stein, S., and M. Wysession (2003). *An Introduction to Seismology, Earthquakes, and Earth Structure*, Blackwell, Oxford, United Kingdom, 498 pp.
- Stiros, S. C., P. A. Pirazzoli, J. Laborel, and F. Laborel-Deguen (1994). The 1953 earthquake in Cephalonia (western Hellenic Arc): Coastal uplift and halotectonic faulting, *Geophys. J. Int.* **117**, no. 3, 834–849, doi: [10.1111/j.1365-246X.1994.tb02474.x](https://doi.org/10.1111/j.1365-246X.1994.tb02474.x).
- Tselentis, G.-A., N. S. Melis, E. Sokos, and P. Beltas (1997). The winter 1991–1992 earthquake sequence at Cephalonia island, western Greece, *Pure Appl. Geophys.* **150**, no. 1, 75–89, doi: [10.1007/s000240050064](https://doi.org/10.1007/s000240050064).
- Underhill, J. R. (1989). Late Cenozoic deformation of the Hellenide foreland, western Greece, *Bull. Geol. Soc. Am.* **101**, no. 5, 613–634, doi: [10.1130/0016-7606\(1989\)101<0613:LCDOTH>2.3.CO;2](https://doi.org/10.1130/0016-7606(1989)101<0613:LCDOTH>2.3.CO;2).
- Valkaniotis, S., A. Ganas, G. Papathanassiou, and M. Papanikolaou (2014). Field observations of geological effects triggered by the January–February 2014 Cephalonia (Ionian Sea, Greece) earthquakes, *Tectonophysics* **630**, 150–157, doi: [10.1016/j.tecto.2014.05.012](https://doi.org/10.1016/j.tecto.2014.05.012).
- Werner, C., U. Wegmuller, T. Strozzi, and A. Wiesmann (2001). Gamma SAR and interferometric processing software, paper presented at *ERS-ENVISAT Symposium*, Gothenburg, Sweden, 15–20 October 2000.
- Wessel, P., and W. H. F. Smith (1998). New, improved version of the Generic Mapping Tools released, *Eos Trans. AGU* **79**, no. 47, 579.
- Weston, J., A. M. G. Ferreira, and G. Funning (2011). Global compilation of interferometric synthetic aperture radar earthquake source models: 1. comparisons with seismic catalogs, *J. Geophys. Res.* **116**, no. B08408, doi: [10.1029/2010JB008131](https://doi.org/10.1029/2010JB008131).
- Weston, J., A. M. G. Ferreira, and G. Funning (2012). Systematic comparisons of earthquake source models determined using InSAR and seismic data, *Tectonophysics* **532/535**, 61–81, doi: [10.1016/j.tecto.2012.02.001](https://doi.org/10.1016/j.tecto.2012.02.001).

John Peter Merryman Boncori

Giuseppe Pezzo

Cristiano Tolomei

Simone Atzori

Stefano Salvi

A. Antonioli

Istituto Nazionale di Geofisica e Vulcanologia

Centro Nazionale Terremoti

Via di Vigna Murata 605

00143 Roma, Italy

john.merryman@ingv.it

giuseppe.pezzo@ingv.it

cristiano.tolomei@ingv.it

simone.atzori@ingv.it

stefano.salvi@ingv.it

andrea.antonioli@ingv.it

Ioannis Papoutsis

Charalampos Kontoes

National Observatory of Athens

Institute of Astronomy, Astrophysics, Space Applications &

Remote Sensing

15236 Athens, Greece

ipapoutsis@space.noa.gr

kontoes@space.noa.gr

Athanasios Ganas

Vassilios Karastathis

Institute of Geodynamics

11810 Athens, Greece

aganas@gein.noa.gr

karastathis@gein.noa.gr

Published Online 19 November 2014